INORGANIC CHEMISTRY
FRONTIERS

RESEARCH ARTICLE

View Article Online
View Journal | View Issue

Cite this: *Inorg. Chem. Front.*, 2025, **12**, 4666

Polyhedral oligomeric silsesquioxane difluoroboron complexes as cooperative octo-site catalysts for the photooxidation of sulfides to sulfoxides†

Mateusz Janeta * and Sławomir Szafert

The incorporation of difluoroboron into the side arms of polyhedral oligomeric silsesquioxanes (POSSs) opens up new possibilities for the construction of metal-free photocatalysts with tailored properties. Herein, we report the design and synthesis of novel difluoroboron complexes of POSSs (**POSS-tert-BF_2**, **POSS-sal-BF_2** and **POSS-npht-BF_2**) derived from imine-functionalized POSSs, which were utilized as efficient photocatalysts. The complexes demonstrated exceptional photocatalytic performance in the aerobic oxidation of sulfides to sulfoxides, significantly outperforming their silsesquioxane-free counterparts. **POSS-tert-BF_2** demonstrated a high singlet oxygen quantum yield of 48%. This study highlights the feasibility of intramolecular cooperative activity in catalytic reactions and identifies key factors influencing its effectiveness. Furthermore, it underscores the potential of POSS as a versatile building block for the development of advanced photocatalytic materials.

Received 1st February 2025,
Accepted 26th March 2025

DOI: 10.1039/d5qi00323g

rsc.li/frontiers-inorganic

Introduction

Polyhedral oligomeric silsesquioxanes (POSSs) have garnered significant attention in materials science due to their unique hybrid inorganic–organic structure and broad range of applications. POSS molecules with the general formula $(RSiO_{3/2})_n$ (where n = 6, 8, 10 or 12 and R can be H, alkyl or aryl) are composed of an inorganic silicon–oxygen cage core (Si–O–Si framework) and organic substituents attached to the silicon atoms. This combination endows POSS-based materials with exceptional thermal stability, mechanical strength, and chemical resistance, making them highly suitable for a wide range of applications including catalysis,[1–5] nanocomposites,[6,7] polymer fillers,[8,9] porous materials,[10,11] and drug delivery systems.[12,13] Beyond the cubic structures, other unique types, including lantern,[14] butterfly,[15] Janus[16] or double-decker[17] shaped cages, have also gained attention for their potential applications.

In a cooperative catalysis system, multiple catalytic moieties operate synergistically, often achieving enhanced catalytic efficiency or specificity compared to noncooperative catalytic systems.[18] Chen *et al.* reported an amphiphilic (salen)Co complex that leverages hydrophobic interactions to enhance the efficiency of a cooperative catalyst.[19]

In the field of silsesquioxanes, we have observed increasing interest in POSS-based systems which could serve as homogenous catalysts. We recently showed that the tetranuclear zinc(II) POSS complex, **Zn_4@POSS-1**, has demonstrated high efficiency as a quattro-site catalyst for the synthesis of cyclic carbonates from epoxides and CO_2 under low-pressure conditions, where the zinc(II) centers in **Zn_4@POSS-1** functioned cooperatively.[20] Furthermore, POSS molecules with imine linkages have been successfully employed in designing porous frameworks, making them highly suitable for applications such as gas storage, adsorption and separation processes, and demonstrating a cooperative effect in iodine capture.[21]

Sulfoxide-containing compounds play a vital role in medicinal chemistry and organic synthesis. They appear in numerous pharmaceuticals (Chart 1) such as omeprazole (a proton-pump inhibitor), modafinil (used for narcolepsy), sulindac (an anti-inflammatory prodrug), and sulforaphane (a natural anticancer agent). Sulfoxides are also present in non-medicinal products like the insecticide fipronil. Consequently, the development of sustainable and selective methods for oxidation of sulfides to sulfoxides is therefore essential in advancing these applications.[22] Oxidation of thioethers has enabled their use in chemical warfare agent (CWA) neutralization.

However, traditional methods for oxidizing organic compounds to synthesize sulfoxides often rely on stoichiometric amounts of toxic heavy metals[23] or highly reactive oxidants,

Faculty of Chemistry, University of Wrocław, F. Joliot-Curie 14, 50-383 Wrocław, Poland. E-mail: mateusz.janeta@uwr.edu.pl

† Electronic supplementary information (ESI) available. See DOI: https://doi.org/10.1039/d5qi00323g

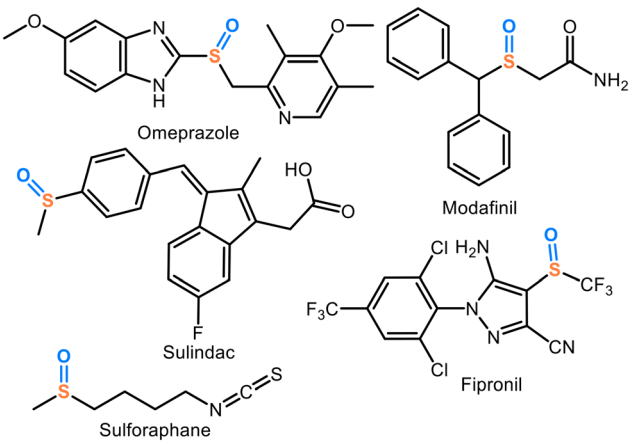

Chart 1 Sulfoxide-containing biologically active compounds.

such as *m*-CPBA, TBHP, UHP, 2-iodobenzoic acid, and oxone or hydrogen peroxide activated by metal catalysts based on tungsten, manganese, copper, iron, molybdenum or gold.[22] These methods require in many cases over-stoichiometric amounts of oxidant and catalysts or operate under high temperatures.

These conventional approaches not only raise serious environmental concerns due to the generation of substantial quantities of toxic byproducts, but they also pose safety risks associated with the handling of hazardous materials. To address these challenges, the photocatalytic activation of molecular oxygen has emerged as a promising green alternative.

BODIPY dyes have proved to be effective in the oxidation of thioanisole.[24–26] Li *et al*. demonstrated that thioanisole can be successfully oxidized to the corresponding sulfoxide within 24 hours, using methanol as the solvent.[24] Later, in 2014, a dimeric BODIPY dye was introduced, significantly enhancing the efficiency of this oxidation reaction and marking a notable advancement in the application of boron-containing dyes for sulfide photooxidation.[27]

Inspired by these findings, we have designed and are presenting herein the synthesis, characterization, and structural investigation of new difluoroboron complexes with POSS as a catalyst for the photooxidation of sulfides to sulfoxides, examining the presence of a cooperative effect.

Results and discussion

Synthesis and characterization of POSS-imine-BF_2

The synthetic pathways for fluoroborate POSS complexes **POSS-imine-BF_2** (where **imine** = **tert**, **sal** or **npht**) are shown in Scheme 1. Imine ligands bearing a POSS moiety (**POSS-1**, **POSS-2**, **POSS-3**, Chart S1, ESI†) were conveniently synthesized by reacting octa(3-aminopropyl)silsesquioxane hydrochloride with the corresponding aldehyde derivative in the presence of triethylamine as a deprotonation agent. Boron complexation was accomplished using boron trifluoride etherate and dry diisopropylethylamine (DIPEA) in dichloromethane at 40 °C, yielding **POSS-imine-BF_2** complexes in high yields. By-products were removed by washing with water. The final products were purified by filtration through a short plug of silica gel using dichloromethane (DCM) and subsequently recrystallized from a DCM/MeOH mixture. It is worth noting that **POSS-imine-BF_2** complexes exhibit excellent stability under ambient conditions and can be stored for several weeks without showing any signs of decomposition. The structures of the complexes were confirmed by (^{1}H, ^{11}B, ^{13}C, ^{19}F, ^{29}Si) NMR, DRIFT, UV-vis spectroscopy, MALDI spectrometry and elemental and TG-DTA analysis.

In the ^{1}H NMR spectrum of **POSS-tert-BF_2** (Fig. 1a), the main indication of complexation is the disappearance of the OH signal at 13.95 ppm which is observed for the free ligand,[20] and a downfield shift of the two doublets attributed to the protons of the phenyl ring, from 7.35 and 7.06 to 7.62 and 7.33 ppm. The ^{1}H NMR spectrum also showed a sharp distinct signal at 8.38 ppm corresponding to the imine group and three signals in the alkyl region at 3.72–3.69, 2.01–1.94, 0.69–0.66 ppm attributed to iminopropyl functional groups. Additionally, two signals at 1.44 and 1.29 were observed, corresponding to the protons of the *tert*-butyl groups (Fig. 1a and Fig. S22, ESI†). Compared to the spectra of the pure ligand, the higher chemical shifts observed for the imine moiety, along with the absence of the broad OH signal, suggest coordination through both the imine and phenoxo groups. This was further corroborated by ^{11}B NMR (Fig. 1b and Fig. S22, ESI†), which showed a peak at 0.49 ppm, which is consistent with the sp^3 boron range and indicates N,O-coordination.[28]

The ^{19}F NMR spectrum (Fig. S25, ESI†) revealed a doublet of doublets at δ = −136.8 ppm, indicating the presence of two diastereotopic fluorine atoms split by a boron atom. The ^{13}C $\{^1$H$\}$ NMR spectrum (Fig. S23, ESI†) matched well with the expected structures, showing a set of symmetry-equivalent signals for the organic side groups. In the DRIFT spectrum (Fig. S30, ESI†) of **POSS-tert-BF_2**, new bands that were absent in the free ligand spectrum appeared at 1308 and 1055 cm^{-1}, attributed to the ν_{B-O} and ν_{B-N} modes, respectively. Bands at 1570, 1150 and 939 cm^{-1} were assigned to the B–F vibrations. The $\nu_{C=N}$ band shifted from 1633 cm^{-1} in the free ligand to 1644 cm^{-1} in **POSS-tert-BF_2**, while the ν_{O-H} stretching vibrations disappeared, indicating that the ligand coordinates *via* the phenol and imine groups. These findings align with the NMR spectroscopy observations (see above). Characteristic vibrations of the Si–O–Si moieties were observed at 1100 cm^{-1}, confirming the presence of a closed silsesquioxane cage structure. The substitution of all side arms in **POSS-tert-BF_2** was unambiguously verified by mass spectrometry. The MALDI mass spectrum (Fig. S31, ESI†) showed a signal at *m*/*z* 3017.4677 $[M + Na]^+$ (calcd 3017.4762), which matched well with the theoretical value, confirming its octametallic structure. Elemental analysis further supported the proposed formulations, and the presence of eight boron atoms per POSS

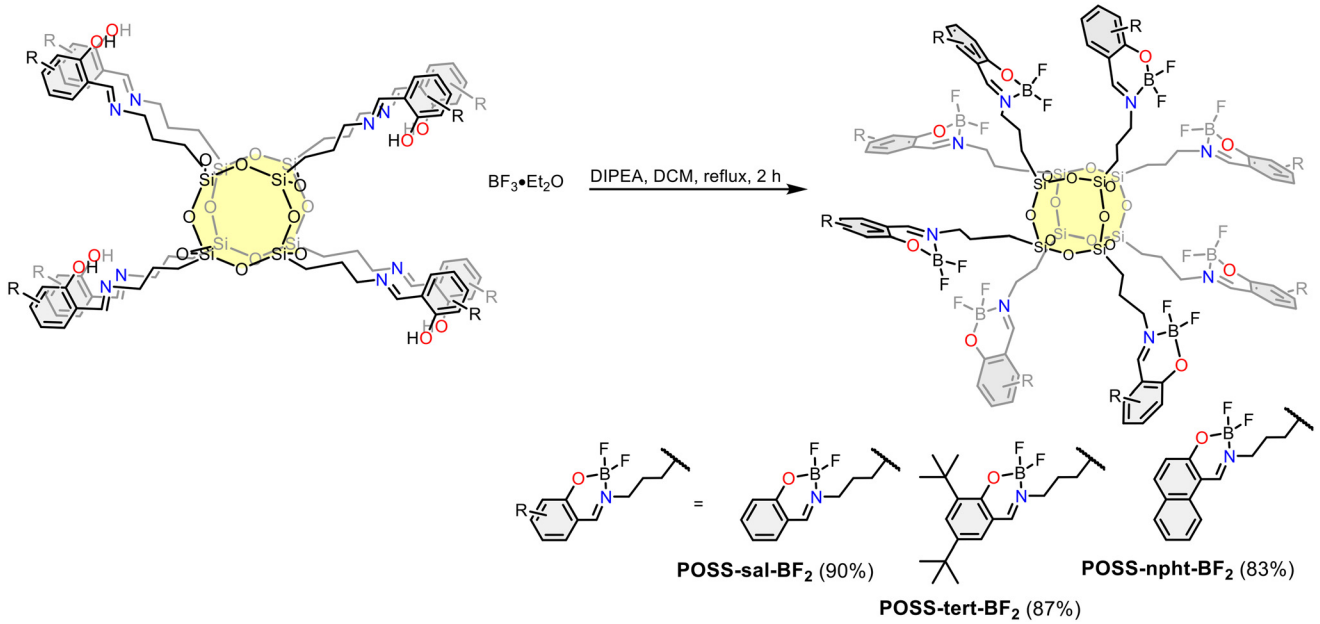

Scheme 1 Synthesis of **POSS-sal-BF_2**, **POSS-tert-BF_2** and **POSS-npht-BF_2**. Isolated yields in parentheses.

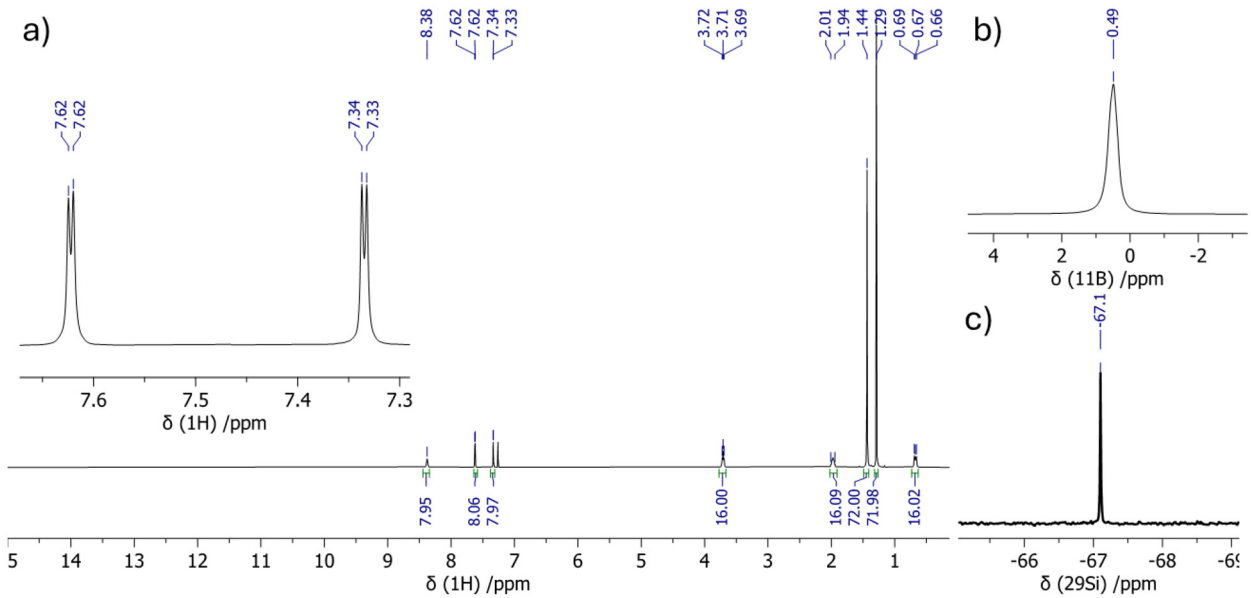

Fig. 1 (a) ^{1}H NMR (500 MHz, $CDCl_3$) spectrum, (b) ^{11}B NMR (160 MHz, $CDCl_3$) spectrum, and (c) ^{29}Si NMR (99 MHz, $CDCl_3$) spectrum of **POSS-tert-BF_2**.

cage was verified using inductively coupled plasma optical emission spectroscopy (ICP-OES).

It is worth noting that reorganization of the POSS cage can occur in the presence of F^- ions, a phenomenon previously observed by Laine *et al.*[29] However, in this study, the integrity of the nanocage was confirmed by the presence of a single resonance in the ^{29}Si NMR spectrum, characteristic of a T_8R_8 structure with T^3 silicon units. The ^{29}Si NMR spectrum of **POSS-tert-BF_2** exhibited a resonance at −67.1 ppm (Fig. 1c, Fig. S26, ESI†), attributed to all eight magnetically equivalent silicon atoms. This observation confirms that no cage rearrangement had occurred and that only a T_8 cage was present in the resulting structure. Further confirmation was provided by diffusion-ordered spectroscopy (DOSY), which supported the nanometer-scale size of the formed structures. The hydrodynamic radii of **POSS-tert-BF_2**, **POSS-sal-BF_2** and **POSS-npht-BF_2** were calculated using the Stokes–Einstein Gierer–Wirtz Estimation (SEGWE) model,[30] yielding approximate

values of 1.15, 1.06, and 1.16 nm, respectively, with diffusion coefficients (D) of 1.13×10^{-10}, 5.10×10^{-10}, and 1.12×10^{-10} m^2 s^{-1}, respectively. Notably, the DOSY spectra exhibited a single, well-defined band for all proton signals, confirming that the POSS structures maintained consistent sizes (Fig. 2, Fig. S27, S40 and S53, ESI†).

Thermal properties

The inorganic framework of polyhedral oligomeric silsesquioxanes (POSSs), specifically the Si–O–Si bonds, enables the exceptional chemical and thermal resistance of these compounds. Compared to purely organic compounds, hybrid organic–inorganic silsesquioxanes exhibit significantly enhanced thermal stability, a critical property for their diverse applications across various fields.

To assess the thermal stability of the difluoroboron complexes **POSS-tert-BF$_2$**, **POSS-sal-BF$_2$**, and **POSS-npht-BF$_2$**, thermogravimetric analysis (TGA) was conducted under oxidative conditions ($O_2 : N_2$ = 40 : 60). The TGA results showed the high thermal resistance of POSSs, depicting 5% weight loss at 350, 335, and 339 °C for **POSS-tert-BF$_2$**, **POSS-sal-BF$_2$**, **POSS-npht-BF$_2$**, respectively (Fig. 3). This remarkable stability can be attributed to the presence of the rigid silsesquioxane cage structure.[31] These findings highlight the excellent thermal stability of the difluoroboron-functionalized POSS compounds and confirm their potential for use in high-temperature applications. The oxidative decomposition of **POSS-tert-BF$_2$**, and of **POSS-sal-BF$_2$** and **POSS-npht-BF$_2$**, proceeded in two distinct steps. The initial weight loss was associated with the decomposition of the organic side chains, while the subsequent weight loss corresponded to degradation of the silsesquioxane cage. Extending the analysis up to 1000 °C under oxidative conditions allowed for determination of the materials' compositions based on their ceramic yields. Notably, pyrolysis of the POSS compounds in air resulted in the formation of silicon oxide (SiO_2), as confirmed by DRIFT analysis. The TGA curve for **POSS-tert-BF$_2$** exhibited a total weight loss of 83.6%, corresponding to a residual SiO_2 content of 16.40%. This value is in close agreement with the theoretical prediction of 15.97%. For **POSS-sal-BF$_2$**, the ceramic yield at 900 °C was found to be 26.17%, exceeding the theoretical value of 22.93%. Similarly, **POSS-npht-BF$_2$** demonstrated a ceramic yield of 22.84%, aligning well with its theoretical value of 19.25%.

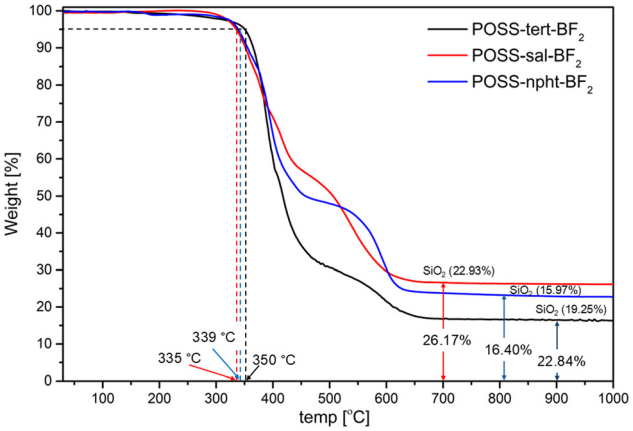

Fig. 3 TGA trace graph (under oxidative conditions) for **POSS-tert-BF$_2$**, **POSS-sal-BF$_2$** and **POSS-npht-BF$_2$**. Theoretical values of ceramic yields are given in parentheses.

Synthesis prop-imine-BF$_2$

To investigate the role of the silsesquioxane cage in photocatalytic activity, we synthesized difluoroboron complexes without the silsesquioxane core, designated as **prop-imine-BF$_2$** (**prop-tert-BF$_2$**, **prop-sal-BF$_2$** and **prop-npht-BF$_2$**, Scheme 2). These compounds were obtained similarly to the POSS-based complexes, using boron trifluoride etherate and dry diisopropylethylamine in dichloromethane at 40 °C. By-products were removed through column chromatography. The structures of the resulting complexes were confirmed by ^{1}H, ^{11}B, ^{13}C and ^{19}F NMR, DRIFT, and UV-vis spectroscopy.

Photophysical properties

In DCM solution, **POSS-tert-BF$_2$**, **POSS-sal-BF$_2$**, and **POSS-npht-BF$_2$** exhibited strong π–π* transition with absorption maxima at 270 nm, 280 nm, and 230 nm, respectively (Fig. 4a). Additional absorption peaks were observed at 367 nm for

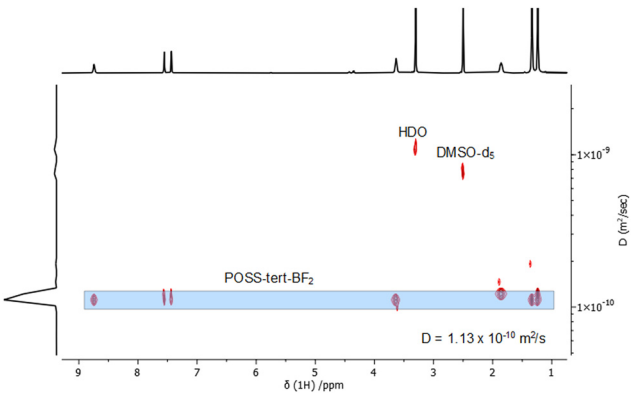

Fig. 2 ^{1}H DOSY NMR (500 MHz, DMSO-d$_6$) spectrum of **POSS-tert-BF$_2$**.

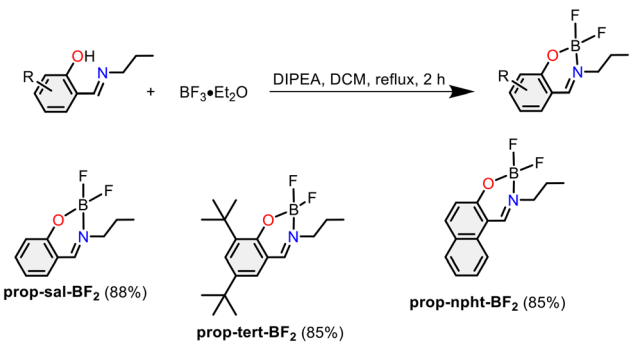

Scheme 2 Synthesis of **prop-tert-BF$_2$**, **prop-sal-BF$_2$** and **prop-npht-BF$_2$**. Isolated yields in parentheses.

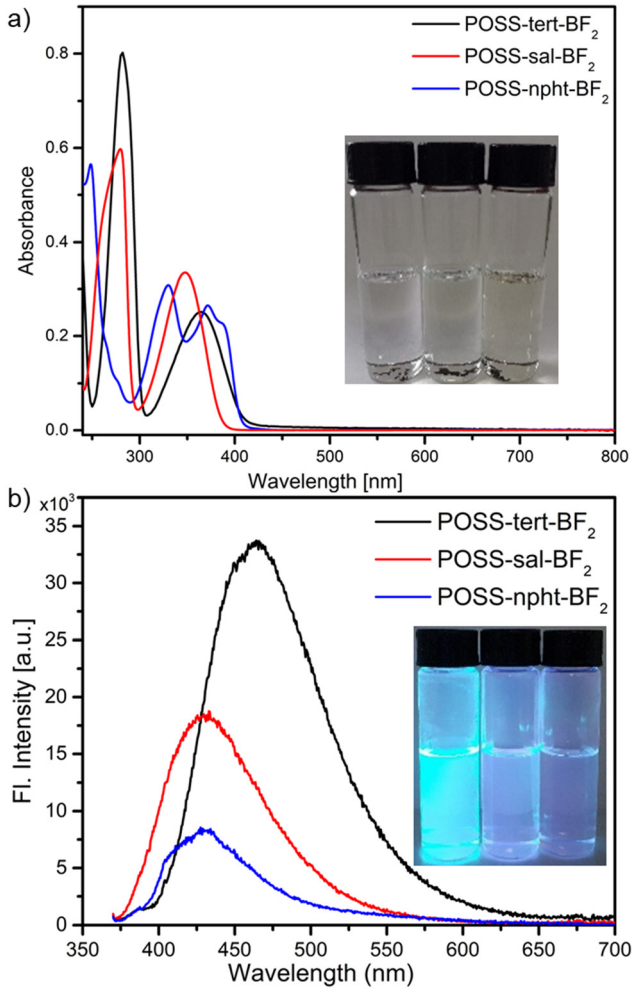

Fig. 4 (a) Electronic absorption spectra (dichloromethane) of **POSS-tert-BF$_2$**, **POSS-sal-BF$_2$** and **POSS-npht-BF$_2$**. Insert: Photograph of **POSS-tert-BF$_2$**, **POSS-sal-BF$_2$** and **POSS-npht-BF$_2$** dichloromethane solutions. (b) Emission spectra of POSSs. Excitation wavelength, 360 nm. Insert: Photograph of fluorescence of **POSS-tert-BF$_2$**, **POSS-sal-BF$_2$** and **POSS-npht-BF$_2$** as observed in dichloromethane solution under UV light irradiation (λ = 365 nm).

Table 1 Absorption and emission properties of **POSS-tert-BF$_2$**, **POSS-sal-BF$_2$** and **POSS-npht-BF$_2$** in CH_2Cl_2

Compound	λ_{abs} (nm)	ε (M^{-1} cm^{-1})	λ_{em} (nm)	Stokes shift (nm)	Φ_f[a] (%)
POSS-tert-BF$_2$	367	26 200	463	98	27.0
prop-tert-BF$_2$	367	4300	463	98	30.9
POSS-sal-BF$_2$	348	32 800	430	82	10.0
prop-sal-BF$_2$	348	4700	426	78	12.0
POSS-npht-BF$_2$	325/372	67 200/63 300	429	100/57[b]	3.6/4.0[b]
prop-npht-BF$_2$	372	7900	428	56	12.0

[a] Determined by comparison with quinine sulfate in 0.1 M H_2SO_4 (Φ_f = 57.7%). Excitation wavelength, 360 nm. [b] Excitation wavelength, 330 nm.

POSS-tert-BF$_2$, 348 for **POSS-sal-BF$_2$**, and 325, 355 and 372 for **POSS-npht-BF$_2$**, which can be attributed to intramolecular charge transfer (ICT) transition (Fig. 4a, Table 1). The formation of the B–N bond, through the donation of a lone pair from the nitrogen atom to the boron atom, reduces the energy gap between the π^* and π orbitals of the ligand, resulting in a bathochromic shift in the UV-vis spectra of **POSS-tert-BF$_2$**, **POSS-sal-BF$_2$** and **POSS-npht-BF$_2$** relative to their respective ligands.

Upon photoexcitation, **POSS-tert-BF$_2$** emitted a bright blue light with a maximum at 463 nm, a quantum yield (Φ_f) of 27%, and a Stokes shift of 98 nm (Fig. 4b, Table 1). In contrast, **POSS-npht-BF$_2$** displayed a faint emission centered at 429 nm with Φ_f = 4%, which is typical of BF_2 complexes with naphthalene ligands.[32] **POSS-sal-BF$_2$** emitted light at 430 nm with a quantum yield of 10%. The incorporation of bulky *tert*-butyl groups in **POSS-tert-BF$_2$** at the periphery of the POSS molecule induced bathochromic shifts in both absorption and emission wavelengths, as well as an increase in the quantum yield compared to **POSS-sal-BF$_2$**. These bulky groups help effectively restrict intramolecular rotations within the organic POSS framework, thereby reducing fluorescence quenching. Interestingly, **POSS-tert-BF$_2$**, **POSS-sal-BF$_2$**, and **POSS-npht-BF$_2$** exhibited lower emission intensities compared to their non-POSS counterparts, **prop-tert-BF$_2$**, **prop-sal-BF$_2$**, and **prop-npht-BF$_2$** (Fig. 4b, Fig. S72 in the ESI,† and Table 1), despite having a larger number of chromophores. This suggests an increased contribution of nonradiative decay pathways, such as self-absorption, due to the higher chromophore density. A similar phenomenon has been previously observed in stilbenevinylsilsesquioxanes.[33] For example, a lower emission intensity (Φ = 11%) was noted for stilbenevinyl-T_{12} compared to stilbenevinyl-T_8 (Φ_f = 36%) and *p*-triethoxysilyl-VS (Φ_f = 38%).

Photocatalytic activity and ROS generation

Having established the efficiency of **POSS-tert-BF$_2$**, we proceeded to evaluate its photocatalytic activity. To investigate the activation effect of **POSS-tert-BF$_2$** on molecular oxygen, 3,3′-dimethylbenzidine (DMB) was used as an indicator for reactive oxygen species (ROS) generation. Upon subjecting a dichloromethane solution of **POSS-tert-BF$_2$** and DMB to constant light irradiation (Herolab NU-15, λ_{irr} = 365 nm, 90 s, intensity 1.30 mW cm^{-2}), characteristic absorption bands of the DMB cation radical[34] appeared at 370 and 650 nm (Fig. 5, Fig. S1, Scheme S1, ESI†). Notably, the oxidation rates of DMB varied significantly under different atmospheric conditions (N_2 and O_2), providing compelling evidence that the reactive oxygen species generated in the system under irradiation indeed originated from molecular oxygen.[35] A similar phenomenon was observed for **POSS-sal-BF$_2$**, **POSS-npht-BF$_2$**, **prop-tert-BF$_2$**, **prop-sal-BF$_2$** and **prop-npht-BF$_2$** confirming their ability to generate ROS during light irradiation (Fig. S2–S6, ESI†).

Singlet oxygen quantum yields

To evaluate the ability of **POSS-tert-BF$_2$** to generate singlet oxygen ($^1O_2$), 9,10-diphenylanthracene (DPA) was employed as

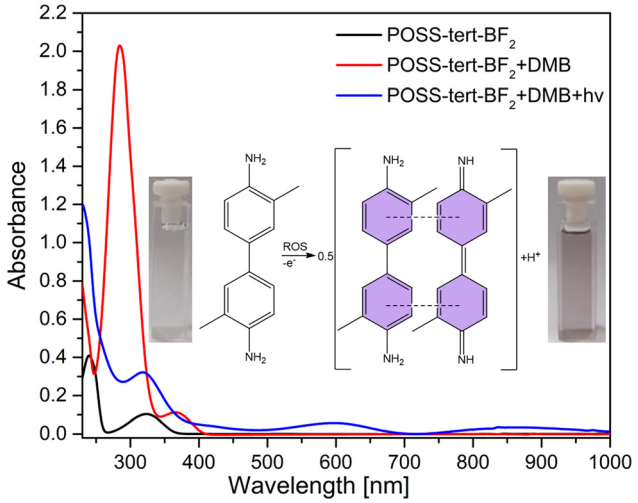

Fig. 5 UV-vis-NIR absorption spectra and photographs of the cationic radical of 3,3′-dimethylbenzidine (DMB) generated by **POSS-tert-BF$_2$** in the presence of light (λ_{irr} = 365 nm, 90 s, intensity 1.30 mW cm^{-2}) and oxygen in DCM. Insert: Photograph of the solution of **POSS-tert-BF$_2$** and DMB in DCM before (left) and after light irradiation (λ_{irr} = 365 nm, 90 s, intensity 1.30 mW cm^{-2}) (right).

a trapping agent. DPA selectively reacts with $^1O_2$, leading to a decrease in its absorbance. Upon irradiating a methanol solution containing DPA and **POSS-tert-BF$_2$**, a reduction in the DPA absorption peak was observed (Fig. 6a), indicating the formation of $^1O_2$. To further confirm this, DPA oxidation experiments were conducted in deuterated methanol (MeOD-d$_4$), as the extended lifetime of $^1O_2$ in a deuterated solvent should enhance DPA oxidation if $^1O_2$ generation occurs. This effect arises because the longer $^1O_2$ lifetime increases the likelihood of its reaction with DPA before relaxing to the ground state. In contrast, when experiments were conducted in the presence of NaN_3, a known $^1O_2$ quencher, no decrease in DPA absorbance was observed, further validating singlet oxygen generation upon **POSS-tert-BF$_2$** irradiation.

The singlet oxygen quantum yield (SOQY, $\Phi(^1O_2)$) was determined by monitoring the photooxidation of DPA in methanol in the presence of POSS derivatives (Fig. S7a–S12a, ESI†). Changes in DPA absorbance at 391 nm were measured over time using low concentrations of photosensitizer and DPA to minimize potential $^1O_2$ quenching by the photocatalyst. SOQYs were calculated by plotting the change in DPA absorbance against irradiation time (see Fig. S7b–S12b, ESI† for details). The calculated $\Phi(^1O_2)$ values for **POSS-tert-BF$_2$**, **POSS-sal-BF$_2$**, **POSS-npht-BF$_2$**, **prop-tert-BF$_2$**, **prop-sal-BF$_2$** and **prop-npht-BF$_2$** were 48%, 35%, 46%, 27%, 26%, and 18%, respectively, highlighting the high efficiency of **POSS-tert-BF$_2$** in generating singlet oxygen. Higher singlet oxygen quantum yield and therefore higher DPA oxidation were obtained for the octametallic **POSS-tert-BF$_2$**, **POSS-sal-BF$_2$**, and **POSS-npht-BF$_2$** than with the monometallic analogues **prop-tert-BF$_2$**, **prop-sal-BF$_2$** and **prop-npht-BF$_2$** under the same reaction conditions, which can be explained by the occurrence of the intramolecular cooperative effect for compounds bearing the POSS moiety, which was further investigated.

Photocatalytic oxidation of sulfides to sulfoxides

Since **POSS-tert-BF$_2$** exhibits a significant singlet oxygen quantum yield and generates other reactive oxygen species, we conducted experiments on photocatalytic oxidation of thioanisole by **POSS-tert-BF$_2$** using medium-pressure mercury lamp. We first inspected the photooxidation of 0.425 mmol of thioanisole in 12 mL of CH_3OH solution with 0.5 mol% **POSS-tert-BF$_2$** (loading based on acceptor sites) as a sensitizer (entry 4 Table 2) at room temperature. Following irradiation with a 150 W TQ lamp (radiation flux ∅ 300–600 nm: 24.8 W), full conversion was achieved within 40 minutes, resulting in a turnover number (TON) of 1582 and a turnover frequency (TOF) of 2373 h^{-1}. The reaction carried out at the mmol scale gave a

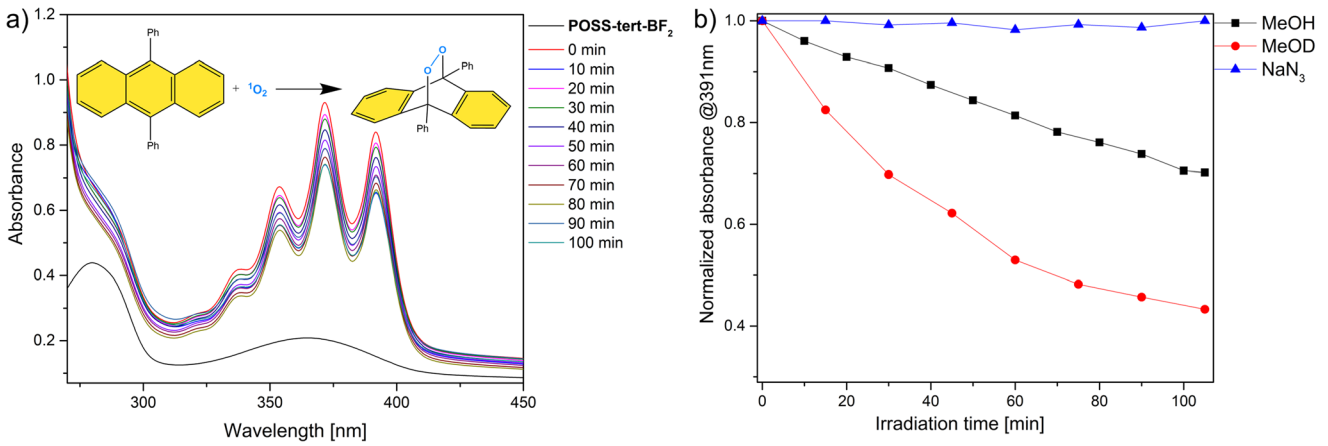

Fig. 6 (a) The absorption spectra of DPA in MeOH after irradiation (λ_{irr} = 365 nm, intensity 1.30 mW cm^{-2}) for different times in the presence of **POSS-tert-BF$_2$**. Inset shows the reaction of DPA with $^1O_2$, generated by irradiation of **POSS-tert-BF$_2$** in the presence of O_2. (b) Plots of Abs (A/A_0) for DPA in MeOH or MeOD-d$_4$ at 391 nm upon light irradiation (λ_{irr} = 365 nm, intensity 1.30 mW cm^{-2}) for different times in the presence of **POSS-tert-BF$_2$** or **POSS-tert-BF$_2$** + NaN_3.

Table 2 Photocatalytic oxidation of thioanisole in the presence of **POSS-imine-BF$_2$** or **prop-imine-BF$_2$** [a]

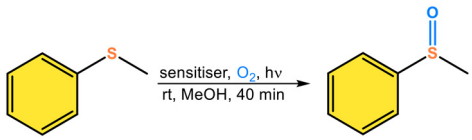

Entry	Photosensitizers	Yield [%]	TON[f]	TOF[g] [h^{-1}]
1	None	0		
2	No light	0		
3	Anaerobic conditions	0		
4	**POSS-tert-BF$_2$**	99	1582	2373
5	**POSS-tert-BF$_2$** [b]	30	479	719
6	**POSS-tert-BF$_2$** [c]	99	794	1905
7	**POSS-tert-BF$_2$** [d]	98	1566	2349
8	**prop-tert-BF$_2$** [e]	65	130	195
9	**POSS-sal-BF$_2$**	70	1118	1678
10	**prop-sal-BF$_2$** [e]	59	118	177
11	**POSS-npht-BF$_2$**	90	1438	2157
12	**prop-npht-BF$_2$** [e]	60	120	180

[a] Reaction conditions: thioanisole (0.425 mmol), **POSS-imine-BF$_2$** (0.266 μmol, 0.0625 mol%, 0.5 mol% based on acceptor sites), MeOH (12 mL), O_2, 40 min, medium pressure mercury vapor lamp (radiation flux ∅ 300–600 nm: 24.8 W), room temperature. [b] DCM as a solvent. [c] Reaction conditions: thioanisole (0.085 mmol), **POSS-tert-BF$_2$** (0.106 μmol, 0.125 mol%, 1 mol% based on acceptor sites), MeOH (2.4 mL), O_2, 25 min, medium pressure mercury vapor lamp (radiation flux ∅ 300–600 nm: 24.8 W), room temperature. [d] Thioanisole (1.0 mmol), **POSS-tert-BF$_2$** (0.63 μmol, 0.0625 mol%, 0.5 mol% based on acceptor sites), MeOH (29 mL), O_2, 40 min. [e] **prop-imine-BF$_2$** (2.13 μmol, 0.5%mol). [f] Turnover number (TON) = total number of moles of thioanisole consumed/mol of catalyst. [g] Turnover frequency (TOF) = TON/time (hours).

yield of 98% (entry 7 Table 2). The external quantum efficiency of thioanisole photooxidation, determined relative to ferrioxalate actinometry in the presence of the **POSS-tert-BF$_2$** system, reached 59%. Control experiments conducted without the photosensitizer, without light, or under anaerobic conditions using a distilled solvent resulted in negligible conversion of thioanisole (entries 1–3, Table 2).

The conversion of thioanisole was only 30% in pure DCM (entry 5, Table 2). However, under the same reaction conditions using MeOH, the conversion increased to 99% (entry 4, Table 2). Protonic solvents, such as MeOH or H_2O, are known to stabilize the intermediate for the formation of $^1O_2$,[36] and, in turn, accelerate photooxidation. These differences in conversion also suggest that $^1O_2$ can be identified as one of the ROS involved in the photooxidation of thioanisole. Comparing the activity of different POSS compounds with various substitutions on the phenyl ring, we observed that introducing steric hindrance, such as with *tert*-butyl groups at the 3- and 5-positions of the phenyl ring in **POSS-tert-BF$_2$**, significantly increased the reaction efficiency (99% in 40 minutes, entry 4, Table 2) compared to **POSS-sal-BF$_2$**, which lacks bulky substituents (70% in 40 minutes, entry 9, Table 2). Furthermore, introducing steric hindrance at the 5,6-positions of the phenyl ring in **POSS-npht-BF$_2$** (entry 11, Table 2) by replacing the phenyl ring with a naphthalene ring also improved efficiency relative to **POSS-sal-BF$_2$**. However, the efficiency remained lower than that of **POSS-tert-BF$_2$**, underscoring the critical role of steric hindrance at the 3-position of the phenyl ring in promoting the conversion of thioanisole. The results indicate that **POSS-tert-BF$_2$** exhibits a high efficiency in photocatalytic oxidation of thioanisole and it was further studied in detail.

The reaction progress was monitored in real time using NMR spectroscopy (Fig. S14, ESI†), which revealed that the conversion of thioanisole to methyl phenyl sulfoxide with **POSS-tert-BF$_2$** as a photosensitizer increased steadily over time, achieving complete conversion within 40 minutes and following zero-order kinetics (Fig. 7). In comparison, the use of **prop-tert-BF$_2$** resulted in only 65% substrate conversion after 40 minutes, with full conversion achieved after 60 minutes. These findings clearly highlight the superior reaction efficiency and faster catalytic performance of **POSS-tert-BF$_2$** compared to **prop-tert-BF$_2$**. Higher conversion (99%) of thioanisole was obtained with the octametallic **POSS-tert-BF$_2$** than with the monometallic analogue **prop-tert-BF$_2$** (65%) under the same reaction conditions, supporting the occurrence of intramolecular cooperative catalysis with **POSS-tert-BF$_2$**. This observation aligns with the observed enhancement in the efficiency of singlet oxygen quantum yields (see above). A similar intramolecular cooperative effect was previously reported for **Zn$_4$@POSS-1**, which contains the **POSS-1** ligand, in the formation of cyclic carbonates from epoxides.[37] A similar enhancement in efficiency was observed for **POSS-sal-BF$_2$** and **POSS-npht-BF$_2$**. Comparing the activity of **POSS-npht-BF$_2$** with **prop-npht-BF$_2$**, a higher yield of 90% *versus* 60% (entries 11 and 12, Table 2), respectively, was obtained for **POSS-npht-BF$_2$**. The activity of **POSS-sal-BF$_2$** is also higher than

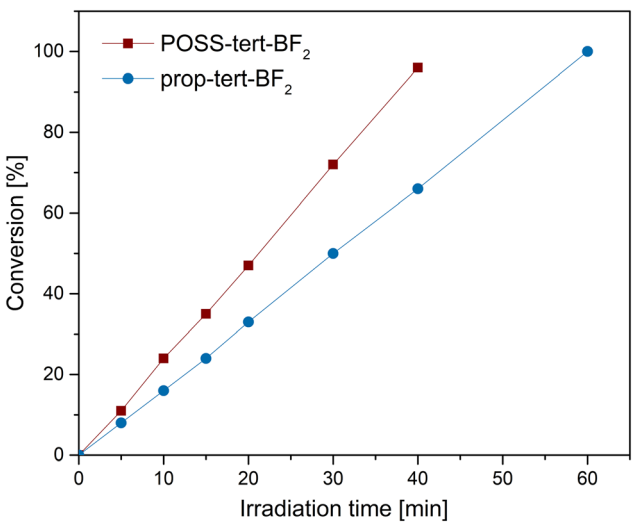

Fig. 7 Kinetic profiles of thioanisole oxidation using **POSS-tert-BF$_2$** (0.796 mg, 0.266 μmol) or **prop-tert-BF$_2$** (0.688 mg, 2.13 μmol) as a photosensitizer. Reaction conditions: thioanisole (0.425 mmol), photosensitizer (0.5 mol% based on acceptor sites), MeOH (12 mL), O_2 (1 atm), medium pressure mercury vapor lamp (radiation flux ∅ 300–600 nm: 24.8 W), and room temperature.

that of **prop-sal-BF$_2$**, 70% *versus* 59% (entries 9 and 10, Table 2).

Recycling of photocatalyst

The recyclability of **POSS-tert-BF$_2$** was evaluated by performing consecutive photocatalytic reactions. **POSS-tert-BF$_2$** retained the majority of its catalytic activity even after five cycles, with conversion rates only slightly decreasing from 99% to 96% (Fig. 8). The post-reaction ^{1}H and ^{11}B NMR spectra (Fig. S73 and S74, ESI†) of **POSS-tert-BF$_2$** were identical to those obtained before the reactions, suggesting that the structural integrity of the catalyst is preserved over multiple cycles. Additionally, ICP-OES analysis of the recovered **POSS-tert-BF$_2$** confirmed that the octametallic structure remained intact, with no detectable boron leaching into the reaction mixture. These findings indicate the robustness and reusability of **POSS-tert-BF$_2$** as a stable photocatalyst under the tested conditions.

Substrate scope

To assess the versatility of **POSS-tert-BF$_2$** as a photocatalyst in the photooxidation of thioanisole derivatives in methanol, a series of substrates with various substituents were evaluated. As illustrated in Scheme 3, thioanisole derivatives containing electron-donating (–CH_3) and electron-withdrawing (–CN, –CHO, –C(O)CH_3) groups achieved high yields of 99%, 82%, 78%, and 96%, respectively. Bromine-substituted derivatives at *ortho* and *meta* positions also exhibited high yields (99%). The low activity of biphenyl sulfide (10%) might be attributed to its steric effect, which prohibits sulfoxide formation and is commonly observed in the literature.[38]

These results underscore the potential of **POSS-tert-BF$_2$** in facilitating thioanisole photooxidation reactions under mild conditions. Notably, nearly complete substrate conversion was achieved within 40 minutes for most derivatives, highlighting the efficiency of **POSS-tert-BF$_2$**. Compared to traditional photocatalysts such as rose bengal,[39] tetra-*o*-acetylriboflavin,[36] and flavin dibromide,[40] which often require extended reaction times or additional promoters, **POSS-tert-BF$_2$** demonstrates superior or comparable performance.

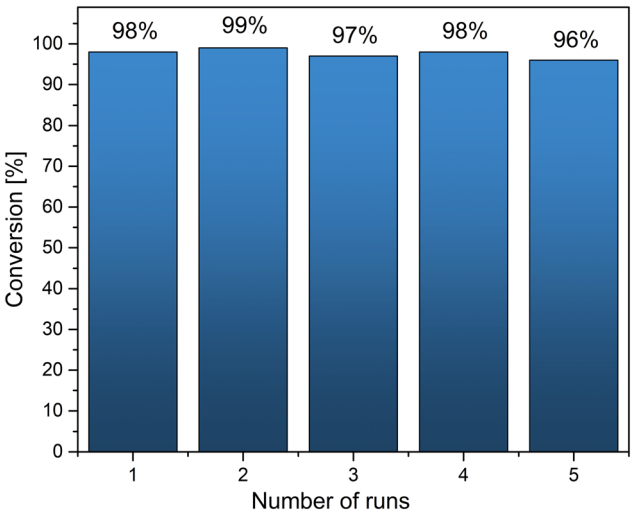

Fig. 8 Recyclability of **POSS-tert-BF$_2$** in sulfide oxidation. Reaction conditions: thioanisole (0.85 mmol), **POSS-tert-BF$_2$** (1.59 mg, 0.532 μmol, 0.5 mol%, loading based on acceptor sites), MeOH (24 mL), O_2 (1 atm), 40 min, medium pressure mercury vapor lamp (radiation flux ⌀ 300–600 nm: 24.8 W), and room temperature.

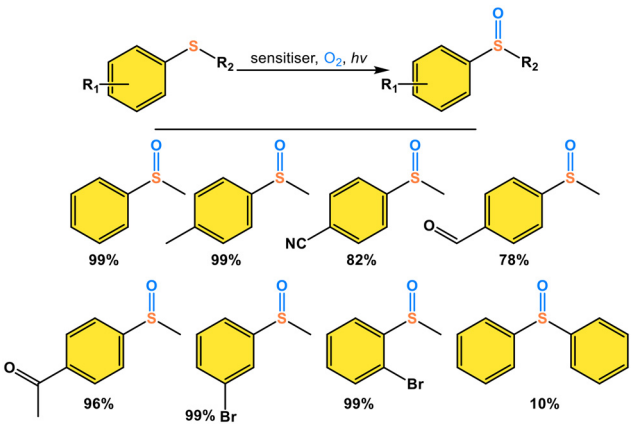

Scheme 3 Photocatalytic selective oxidation of various sulfides to sulfoxides, R_1 = aryl group, R_1 = methyl or phenyl group. Reaction conditions: sulfides (0.430 mmol), **POSS-tert-BF$_2$** (0.796 mg, 0.266 μmol, 0.5 mol%, loading based on acceptor sites), MeOH (12 mL), O_2, medium pressure mercury vapor lamp (radiation flux ⌀ 300–600 nm: 24.8 W), and room temperature, yields of isolated products.

Quenching experiments

To investigate the process and the reactive species involved in the photocatalytic oxidation of sulfides to sulfoxides, we conducted separate experiments using individual free radical or singlet oxygen scavengers. They included KI, NaN_3, DABCO, and 1,4-benzoquinone (BQ), which are used to eliminate holes (h^+), singlet oxygen ($^1O_2$), and superoxide anion radicals ($O_2^{\bullet-}$), respectively. As depicted in Fig. 9, the incorporation of KI, NaN_3, and DABCO led to a significant reduction in the yield of the oxidation reaction, resulting in yields of 11%, 11%, and 19% respectively. The inclusion of BQ under the same reaction conditions reduced conversion to 56%. This observation implies that $^1O_2$ and h^+ function as the principal active species in the photocatalytic oxidation of sulfides to sulfoxides. Therefore, **POSS-tert-BF$_2$** acts as both a type I and a type II photocatalyst. A plausible mechanism for oxidation of sulfides is provided based on the findings from the aforementioned studies and relevant literature sources.[38,41] With the results of quenching experiments, conducted to determine the impact of ROS, the likely reaction mechanisms proposed are shown in Scheme 4. **POSS-tert-BF$_2$** is first photoexcited, generating photogenerated electron–hole pairs upon light irradiation, which then oxidize sulfides into cationic free radicals. The separated electrons reduce O_2 to form reactive oxygen species ($O_2^{\bullet-}$). Then sulfide cation free radicals can react with $O_2^{\bullet-}$ to form a persulfoxide intermediate. Simultaneously, the sulfide

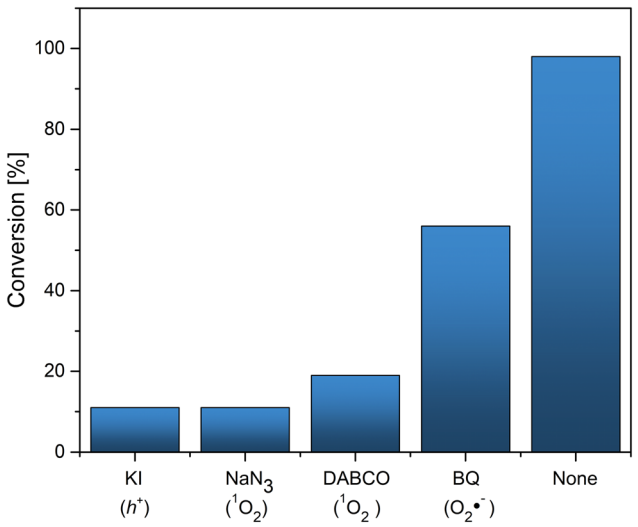

Fig. 9 Control experiments for thioanisole oxidation in the presence of different scavengers: KI, NaN_3, DABCO, or BQ. Reaction conditions: thioanisole (0.085 mmol), **POSS-tert-BF$_2$** (0.159 mg, 0.053 μmol, 0.5 mol% based on acceptor sites), scavenger (0.17 mmol), MeOH (2.4 mL), O_2 (1 atm), 40 min, medium pressure mercury vapor lamp (radiation flux ∅ 300–600 nm: 24.8 W), and room temperature.

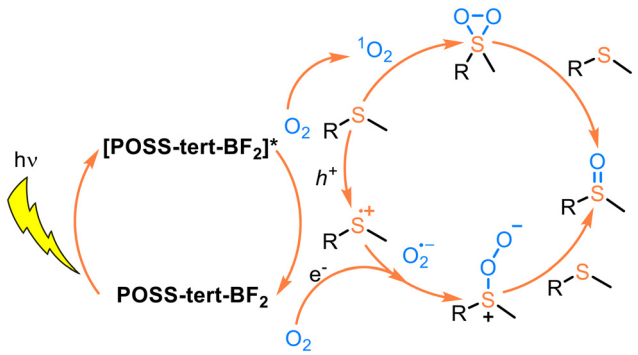

Scheme 4 Proposed reaction mechanisms of sulfide-selective oxidation by **POSS-tert-BF$_2$** in the presence of O_2.

can react with singlet oxygen ($^1O_2$) to form a thiadioxirane intermediate. In the final step, both of these reaction intermediates react with another sulfide molecule to yield sulfoxide.

Conclusion

In summary, a new type of octanuclear difluoroboron coordination compound was designed and synthesized through a reaction of boron trifluoride etherate with imine functionalized polyhedral silsesquioxanes. For the first time, multifunctional imine-POSS-based difluoroboron complexes were synthesized and characterized. **POSS-tert-BF$_2$**, **POSS-sal-BF$_2$**, and **POSS-npht-BF$_2$** were successfully tested in the photooxidation of sulfides to sulfoxide, demonstrating high activity and selectivity of the tested catalytic system. Thioanisole was converted under mild conditions (room temperature) and with a short reaction time (40 minutes) into sulfoxide in high yield (99%). High yields were also obtained for thioanisole derivatives containing both electron-donating and electron-withdrawing groups, showcasing the versatility of the obtained system.

Moreover, we have demonstrated the first example of an intramolecular cooperative catalytic system for the photooxidation of sulfides to sulfoxides. This was achieved through the unique properties of the silsesquioxane core in POSS compounds. Our study highlights several advantages of POSS-based photocatalysts, which make them particularly suitable for the photooxidation of sulfides to sulfoxides.

- High photostability: the silsesquioxane core provides durability against oxidation, which enhances the longevity of the catalyst.
- High singlet oxygen $^1O_2$ generation ability: a high singlet oxygen quantum yield of 48% in MeOH was achieved for **POSS-tert-BF$_2$**.
- High efficiency: the higher TON in relation to non-POSS analogues was caused by the intramolecular cooperative effect.
- Environmentally friendly system: the photocatalyst does not contain heavy metals and does not require highly reactive oxidants, toxic byproducts are not produced, and oxidation occurs under oxygen.

Materials and methods

All information regarding the synthesis, chemical characterization, experimental details and materials used in this study have been included as part of the ESI.†

Author contributions

Conceptualization, M. J. and S. S. Data curation, M. J. Validation, M. J. Formal analysis, M. J. Funding acquisition, M. J. and S. S. Investigation, M. J. Methodology, M. J. Visualization, M. J. Writing – original draft, M. J. Writing – review & editing, M. J.

Data availability

The data supporting this article have been included as part of the ESI.† It contains materials, structures of POSS ligands, characterization methods, syntheses, description of experiments. UV-vis spectra of DPA upon light irradiation in presence of photocatalysts, UV-vis-NIR spectra of the cationic radical of DMB generated upon light irradiation in the presence of photocatalysts, ^{1}H NMR spectra of crude mixtures for oxidation of thioanisole using **POSS-tert-BF$_2$**, ^{1}H NMR spectra of photooxidation products, ^{1}H, ^{13}C, ^{11}B, ^{19}F, ^{29}Si, DOSY, NOESY and HSQC NMR, DRIFT, UV-vis spectra, MALDI mass spectra, and TG-DTA data.

Conflicts of interest

There are no conflicts to declare.

Acknowledgements

The authors acknowledge the National Science Centre 2022/45/B/ST4/01511 (S. S.) and University of Wrocław for the BPIDUB.12.2024 (M. J.) grant under the 'The Excellence Initiative – Research University' programme for support of this research. M. J. gratefully acknowledges the financial support by the Ministry of Education and Science through the scholarship for outstanding young scientists (SMN/16/1767/2020/3).

References

1 V. Ervithayasuporn, K. Kwanplod, J. Boonmak, S. Youngme and P. Sangtrirutnugul, Homogeneous and heterogeneous catalysts of organopalladium functionalized-polyhedral oligomeric silsesquioxanes for Suzuki–Miyaura reaction, *J. Catal.*, 2015, **332**, 62–69.

2 Y. Liu, K. Koizumi, N. Takeda, M. Unno and A. Ouali, Synthesis of octachloro- and octaazido-functionalized T_8-cages and application to recyclable palladium catalyst, *Inorg. Chem.*, 2022, **61**, 1495–1503.

3 C. Calabrese, C. Aprile, M. Gruttadauria and F. Giacalone, POSS nanostructures in catalysis, *Catal. Sci. Technol.*, 2020, **10**, 7415–7447.

4 C. Sun and H. Liu, Highly selective oxidation of styrene to styrene oxide over a tetraphenylporphyrin-bridged silsesquioxane-based hybrid porous polymer, *ACS Appl. Polym. Mater.*, 2022, **4**, 5471–5481.

5 A. B. Soni, G. Satishkumar and M. W. C. Man, Palladium nanoparticles stabilized in ionic liquid-based periodic mesoporous organosilica: An efficient heterogeneous catalyst for oxidative acylation of ketones, *ChemistrySelect*, 2024, **9**, e202403464.

6 Y. Rodriguez Herrero and A. Ullah, Hydrophobic polyhedral oligomeric silsesquioxane support enhanced methanol production from CO_2 hydrogenation, *ACS Appl. Mater. Interfaces*, 2023, **15**, 14399–14414.

7 M. Mansourian-Tabaei, M. Majdoub, D. Sengottuvelu, D. L. Stoddard, R. V. K. G. Thirumalai, M. G. Ucak-Astarlioglu, A. Al-Ostaz and S. Nouranian, Polyurea/aminopropyl isobutyl polyhedral oligomeric silsesquioxane-functionalized graphene nanoplatelet nanocomposites for force protection applications, *ACS Appl. Mater. Interfaces*, 2024, **16**, 19625–19641.

8 T. Hamada, Y. Nakanishi, K. Okada, S. Tsukada, A. Uedono and J. Ohshita, Thermal insulating property of silsesquioxane hybrid film induced by intramolecular void spaces, *ACS Appl. Polym. Mater.*, 2021, **3**, 3383–3391.

9 X. Meng, Y. Liu, S. Wang, J. Du, Y. Ye, X. Song and Z. Liang, Silsesquioxane–carbazole-corbelled hybrid porous polymers with flexible nanopores for efficient CO_2 conversion and luminescence sensing, *ACS Appl. Polym. Mater.*, 2020, **2**, 189–197.

10 H. Yang and H. Liu, Pyrene-functionalized silsesquioxane as fluorescent nanoporous material for antibiotics detection and removal, *Microporous Mesoporous Mater.*, 2020, **300**, 110135.

11 Q. Wang, M. Unno and H. Liu, Ultrafast and highly selective gold recovery with high capture capacity from electronic waste by upconversion of a silsesquioxane-based hybrid luminescent aerogel, *J. Mater. Chem. A*, 2024, **12**, 5679–5691.

12 G. Wei, K. Zhang, Y. Gu, S. Guang, J. Feng and H. Xu, Novel multifunctional nano-hybrid polyhedral oligomeric silsesquioxane-based molecules with high cell permeability: molecular design and application for diagnosis and treatment of tumors, *Nanoscale*, 2021, **13**, 2982–2994.

13 L. Fan, X. Wang, Q. Cao, Y. Yang and D. Wu, POSS-based supramolecular amphiphilic zwitterionic complexes for drug delivery, *Biomater. Sci.*, 2019, **7**, 1984–1994.

14 T. Uchida, Y. Egawa, T. Adachi, N. Oguri, M. Kobayashi, T. Kudo, N. Takeda, M. Unno and R. Tanaka, Synthesis, structures, and thermal properties of symmetric and Janus "lantern cage" siloxanes, *Chem. – Eur. J.*, 2019, **25**, 1683–1686.

15 N. Oguri, Y. Egawa, N. Takeda and M. Unno, Janus-cube octasilsesquioxane: Facile synthesis and structure elucidation, *Angew. Chem., Int. Ed.*, 2016, **55**, 9336–9339.

16 A. Blázquez-Moraleja, M. E. Pérez-Ojeda, J. R. Suárez, M. L. Jimeno and J. L. Chiara, Efficient multi-click approach to well-defined two-faced octasilsesquioxanes: the first perfect Janus nanocube, *Chem. Commun.*, 2016, **52**, 5792–5795.

17 A. Mrzygłód, M. P. García Armada, M. Rzonsowska, B. Dudziec and M. Nowicki, Metallodendrimers unveiled: Investigating the formation and features of double-decker silsesquioxane-based silylferrocene dendrimers, *Inorg. Chem.*, 2023, **62**, 16932–16942.

18 M. A. Stevens and A. L. Colebatch, Cooperative approaches in catalytic hydrogenation and dehydrogenation, *Chem. Soc. Rev.*, 2022, **51**, 1881–1898.

19 P. Solís-Muñana, J. Salam, C. Z.-J. Ren, B. Carr, A. E. Whitten, G. G. Warr and J. L.-Y. Chen, An amphiphilic (salen)Co complex – Utilizing hydrophobic interactions to enhance the efficiency of a cooperative catalyst, *Adv. Synth. Catal.*, 2021, **363**, 3207–3213.

20 M. Janeta, T. Lis and S. Szafert, Zinc imine polyhedral oligomeric silsesquioxane as a quattro-site catalyst for the synthesis of cyclic carbonates from epoxides and low-pressure CO_2, *Chem. – Eur. J.*, 2020, **26**, 13686–13697.

21 M. Janeta, W. Bury and S. Szafert, Porous silsesquioxane–imine frameworks as highly efficient adsorbents for cooperative iodine capture, *ACS Appl. Mater. Interfaces*, 2018, **10**, 19964–19973.

22 E. Skolia, P. L. Gkizis and C. G. Kokotos, Aerobic photocatalysis: Oxidation of sulfides to sulfoxides, *ChemPlusChem*, 2022, **87**, e202200008.

23 K. Kamata, K. Sugahara, Y. Kato, S. Muratsugu, Y. Kumagai, F. Oba and M. Hara, Heterogeneously catalyzed aerobic oxidation of sulfides with a $BaRuO_3$ nanoperovskite, *ACS Appl. Mater. Interfaces*, 2018, **10**, 23792–23801.
24 W. Li, Z. Xie and X. Jing, BODIPY photocatalyzed oxidation of thioanisole under visible light, *Catal. Commun.*, 2011, **16**, 94–97.
25 H. Wang, G. W. Wagner, A. X. Lu, D. L. Nguyen, J. H. Buchanan, P. M. McNutt and C. J. Karwacki, Photocatalytic oxidation of sulfur mustard and its simulant on BODIPY-incorporated polymer coatings and fabrics, *ACS Appl. Mater. Interfaces*, 2018, **10**, 18771–18777.
26 X.-L. Li, N. Han, R.-Z. Zhang, K.-K. Niu, R.-Z. Dong, H. Liu, S. Yu, Y.-B. Wang and L.-B. Xing, Host–guest photosensitizer of a cationic BODIPY derivative and cucurbit[7]uril for high-efficiency visible light-induced photooxidation reactions, *ACS Appl. Mater. Interfaces*, 2023, **15**, 55803–55812.
27 L. Wang, J. Cao, J. Wang, Q. Chen, A. Cui and M. He, Facile synthesis of dimeric BODIPY and its catalytic activity for sulfide oxidation under visible light, *RSC Adv.*, 2014, **4**, 14786–14790.
28 R. Kumar Yadav, D. Parveen, B. Mondal and D. Kumar Roy, The role of spacers as a probe in variation of photoluminescence properties of mono- and bi-nuclear boron compounds, *Chem. – Asian J.*, 2025, **20**, e202401113.
29 J. C. Furgal, T. G. Iii and R. M. Laine, D_{5h} $[PhSiO_{1.5}]_{10}$ synthesis via F− catalyzed rearrangement of $[PhSiO1.5]_n$. An experimental/computational analysis of likely reaction pathways, *Dalton Trans.*, 2016, **45**, 1025–1039.
30 R. Evans, G. Dal Poggetto, M. Nilsson and G. A. Morris, Improving the interpretation of small molecule diffusion coefficients, *Anal. Chem.*, 2018, **90**, 3987–3994.
31 M. Janeta and S. Szafert, Synthesis, characterization and thermal properties of T_8 type amido-POSS with *p*-halophenyl end-group, *J. Organomet. Chem.*, 2017, **847**, 173–183.
32 R. P. Nandi, P. Sudhakar, N. K. Kalluvettukuzhy and P. Thilagar, Triarylborane-appended anils and boranils: solid-state emission, mechanofluorochromism, and phosphorescence, *Chem. – Eur. J.*, 2020, **26**, 16306–16317.
33 J. C. Furgal, J. H. Jung, T. Goodson and R. M. Laine, Analyzing structure–photophysical property relationships for isolated T_8, T_{10}, and T_{12} stilbenevinylsilsesquioxanes, *J. Am. Chem. Soc.*, 2013, **135**, 12259–12269.
34 P. D. Josephy, Oxidative activation of benzidine and its derivatives by peroxidases., *Environ. Health Perspect.*, 1985, **64**, 171–178.
35 H. Zhai, Z. Wei, X. Jing and C. Duan, A porphyrin-faced Zn_8L_6 cage for selective oxidation of $C(sp^3)$–H bonds and sulfides, *Inorg. Chem.*, 2024, **63**, 14375–14382.
36 J. Dad'ová, E. Svobodová, M. Sikorski, B. König and R. Cibulka, Photooxidation of sulfides to sulfoxides mediated by tetra-O-acetylriboflavin and visible light, *ChemCatChem*, 2012, **4**, 620–623.
37 S. Akine, T. Taniguchi and T. Nabeshima, Cooperative formation of trinuclear zinc(II) complexes via complexation of a tetradentate oxime chelate ligand, salamo, and zinc(II) acetate, *Inorg. Chem.*, 2004, **43**, 6142–6144.
38 W. Gong, X. Deng, K. Dong, L. Liu and G. Ning, A boranil-based conjugated microporous polymer for efficient visible-light-driven heterogeneous photocatalysis, *Polym. Chem.*, 2021, **12**, 3153–3159.
39 X. Gu, X. Li, Y. Chai, Q. Yang, P. Li and Y. Yao, A simple metal-free catalytic sulfoxidation under visible light and air, *Green Chem.*, 2013, **15**, 357–361.
40 C. Dang, L. Zhu, H. Guo, H. Xia, J. Zhao and B. Dick, Flavin dibromide as an efficient sensitizer for photooxidation of sulfides, *ACS Sustainable Chem. Eng.*, 2018, **6**, 15254–15263.
41 Y. Liu, Z. Zhao, W. Xu and W. Gong, Extending 2D covalent organic frameworks by inserting anthracene for promoted white-light-mediated photocatalysis, *Catal. Sci. Technol.*, 2024, **14**, 3211–3218.

